Supporting Information

Rational Construction of Loosely Packed Nickel Nanoparticulate with Residual HCOO Ligands Derived from Ni-MOF for High-Efficiency Electrocatalytic Overall Water Splitting

Shumin Wang,[a1] Yi Zhang,[a1] Xiaoyang Deng,[a] Zizai Ma,[bc] Rentao Cheng,[a] Zihao Wan,[a] Jinping Li,[b] and Xiaoguang Wang*[ab]

a Laboratory of Advanced Materials and Energy Electrochemistry, Institute of New Carbon Materials, College of Material Science and Engineering, Taiyuan University of Technology, Taiyuan, 030024, China. E-mail: wangxiaoguang@tyut.edu.cn; wangxiaog1982@163.com

b Shanxi Key Laboratory of Gas Energy Efficient and Clean Utilization, Taiyuan University of Technology, Taiyuan, 030024, China.

c College of Chemistry, Taiyuan University of Technology, Taiyuan, 030024, China

1 These authors contributed equally

Experimental Section

1. Materials and chemicals

All chemicals purchased were reagent grade and without further purification. Nickel nitrate hexahydrate ($Ni(NO_3)_2 \cdot 6H_2O$), formic acid [FA, HCOOH], Pt/C (20 wt. %), RuO_2 and Nafion (5 wt. %) were supplied by Shanghai Aladdin Biochemical Technology Co., Ltd. N,N-dimethylformamide (DMF), acetone, potassium hydroxide (KOH), hydrogen chloride (HCl), and absolute ethanol were received from Tianjin Kermel Chemical Reagent Co. Ltd. NF (nickel foam) (void ratio > 98%, ppi: 110) was

purchased from Kunshan Jiayisheng Electronics Co. Ltd. Ultrapure water (18.2 MΩ cm) was obtained using an UPT-II purification system and used in all the experiments.

2. Synthesis of electrocatalysts

2.1 Synthesis of Ni-MOF@NF precursor

The Ni-MOF microarray was synthesized on NF by a facile solvothermal method according to the previous work.[1] In a typical method, a piece (2.5 cm × 3 cm) of NF was firstly sonicated in 1.0 M HCl, ethanol and DI water for 10 min, respectively. Then, 4.8 mmol $Ni(NO_3)_2 \cdot 6H_2O$ and 32.4 mmol FA were added in 20 mL DMF solution and vigorously stirred for 30 min to form a homogeneous solution. The obtained solution was transferred into a 25 mL of Teflon-lined stainless autoclave, and the cleaned NF was vertically immersed into the solution. Subsequently, the autoclave was sealed and heated in an oven at 100 °C for 12 h. The precursor product ($[Ni_3(HCOO)_6]$ on NF) was rinsed thoroughly with DMF and acetone several times and dried at 60 °C, which was labeled as Ni-MOF@NF.

2.2 Preparation of Ni-250-2@NF catalyst

Briefly, the as-prepared Ni-MOF@NF precursor was placed in the middle of the quartz tube furnace. The H_2/Ar (5% H_2 and 95% Argon) gas was firstly flowed through the tube for 10 min to evacuate the air. Then, the furnace was heated up to 250 °C for 2 h at a ramp rate of 5 °C min^{-1}. Finally, after the furnace was naturally cooled down to room temperature, the obtained sample was denoted as Ni-250-2@NF. Noted that the mass loading of active material on NF is ca. 4.0 mg cm^{-2}.

2.3 Preparation of Ni-250-12@NF catalyst

For the comparison, the Ni-250-12@NF was synthesized by calcining the Ni-MOF@NF precursor in a muffle furnace at 250 °C for 12 h.

2.4 Preparation of Ni-*T*@NF catalyst

The Ni-*T*@NF (*T* = 400 and 550 °C) samples was also prepared using a similar method by calcining Ni-MOF@NF at 400 and 550 °C for 2 h, respectively.

2.5 Preparation of p-Ni@NF catalyst

The p-Ni@NF sample was prepared using electrodeposition method. In detail, an aqueous mixture of 0.2 M $NiCl_2$ and 4.5 M NH_4Cl was stirred for 30 min to obtain the uniform electrolyte. The as-cleaned NF and graphite rod were immersed into the electrolyte as working electrode and counter electrode, respectively. The electrodeposition was galvanostatic at 0.4 A cm^{-2} for 10 min. After electrodeposition, the p-Ni@NF sample was rinsed in ethanol and vacuum-dried overnight at 60 °C.

2.6 Preparation of Pt/C/NF, RuO_2/NF and testing electrodes

5 mg of the Pt/C (20 wt. %) was added into a mixed solution consisting of isopropyl alcohol (1 mL) and 5 wt% Nafion solution (20 μL). After an ultrasonic treatment for more than 30 min, the catalyst ink was coated onto the bare NF with a Pt/C loading amount equal to the active mass of as-prepared catalysts (4 mg cm^{-2}). And the commercial RuO_2/NF electrode was also made via a similar process.

To prepare the Ni-250-2@NF electrode, the dried Ni-250-2@NF (2.5 cm × 3 cm) was cut into 1 cm × 1 cm for subsequent electrochemical test. The electrodes of other samples (Ni-250-12@NF, Ni-400@NF, Ni-550@NF and p-Ni@NF, etc.) for HER and OER were also prepared using the same procedure.

3. Microstructure characterization

X-ray powder diffraction (XRD) patterns were recorded from 5° to 90° by DX-2700 X-ray diffractometer (XRD) with a diffractometer of Cu-Ka (λ = 0.154059 nm) at 40 kV and 30 mA. Thermal gravimetric analysis (TGA) of Ni-MOF powders were carried out using a TG 209 F3 in a nitrogen atmosphere (200 mL min^{-1}) in order to determine the optimum calcination temperature. Scanning electron microscopy (SEM) images were taken by a GeminiSEM 300 machine. Transmission electron microscopy (TEM), high-resolution transmission electron microscopy (HRTEM) and energy dispersive X-ray spectroscopy (EDX) for elemental mapping was also carried out utilizing a JEM-2010F instrument at an accelerating voltage of 200 kV. The chemical states of the samples were measured by X-ray photoelectron spectroscopy (XPS) using ESCALAB 250 apparatus, equipped by micro-focused Al K-alpha as an X-ray source, and the C1s (284.8 eV) was used as the calibration reference. FT-IR spectra of the samples were performed on Bruker tensor II Fourier transform infrared spectrometer in transmittance mode and the frequency range was from 400 cm^{-1} to 4000 cm^{-1}, with a spectral resolution of 4 cm^{-1}. X-ray absorption fine structure (XAFS) spectra were collected using an Easy XES150 system (Easy XAFS LLC, USA), and the data were analyzed by the Athena and hama software.[2] The hard X-ray was monochromatized with a Si (551) crystal monochromator and air-cooled tube with Pd outputting at 25 kV and 2 mA. The Brunauer-Emmett-Teller (BET) surface areas were determined from nitrogen adsorption isotherms at 77 K (3H-2000 PM2). The pore size distribution was computed from the adsorption branches of isotherms by the Barrett-Joyner-Halenda

method. The contact angles were measured by a SL200B analyzer (Solon Tech. (Shanghai) Co., Ltd.) to evaluate the surface wettability. After 2 μL of 1.0 M KOH solution dropped on the sample surface, the equipped camera system would capture a photo, according to which the contact angle was measured.

4. Electrochemical measurements

The electrochemical measurements were carried out at room temperature using the CS-350 electrochemical workstation in a standard three-electrode system with Hg/HgO (1.0 M KOH), carbon rod, and the synthesized catalysts as the reference, counter and working electrodes, respectively. Before each electrochemical measurement, the electrolytes were deaerated by bubbling of N_2 for 30 min to avoid any possible occurrence of oxygen reduction. Before evaluating the activity for HER and OER, all catalysts were activated by 30 cyclic voltammetry (CV) cycles across the potential window (-1.844 ~ -0.496 V for HER and 0.924 ~ 2.424 V for OER) at a scan rate of 20 mV s^{-1} to reach a steady state. In a N_2-saturated 1.0 M KOH solution, the polarization curves were obtained using linear sweep voltammetry (LSV) with a scan rate of 5 mV s^{-1} for HER and 2 mV s^{-1} for OER, and all the polarization curves were corrected for 80% iR compensation. All the potentials measured versus Hg/HgO were calibrated to reversible hydrogen electrode (RHE) according to the Nernst equation:[3]

$$E\ (RHE) = E\ (Hg/HgO) + 0.098\ V + 0.059\ pH \quad (1)$$

The Tafel plots were measured at 1 mV s^{-1} and the slopes were calculated based on the equation:

$$\eta = b \log j + a \quad (2)$$

where η, b and j are the overpotential, Tafel slope and current density, respectively. Electrochemical impedance spectroscopy (EIS) measurement was performed from the frequency of 100 kHz to 0.1 Hz at the potential of -0.126 V (vs. RHE) for HER and 1.604 V (vs. RHE) for OER with a 10 mV sinusoidal perturbation. To evaluate the electrochemical active surface area (ECSA) of these electrodes, double-layer capacitance measurements (C_{dl}) were carried out in the potential region from 0.774 V to 0.874 V (vs. RHE) for HER and 0.924 V to 1.024 V (vs. RHE) for OER from the CV curves without faradaic process at different scan rates (20, 40, 60, 80, 100 and 120 mV s^{-1}). Generally, the ECSA is calculated based on the following equation:

$$\text{ECSA} = \frac{C_{dl}}{C_s} \tag{3}$$

Where C_s is the specific capacitance of the sample or the capacitance of an atomically smooth planar surface of the material per unit area under identical electrolyte conditions. Generally, due to the specific capacitance of anatomically smooth planar surface with a real surface area of 1.0 cm^2, the specific capacitance (C_s) is calculated within 20-60 μF cm^{-2} in alkaline media. In this study, the number of 40 μF cm^{-2} is used as the general specific capacitance of C_s in 1.0 M alkaline media alike the reported in many previous literatures.[3]

In order to investigate the influence of ECSA on the electrocatalytic performance, the HER and OER curves were normalized by ECSAs. The ECSA-normalized current density for the catalysts was calculated by the following equation:[4-6]

$$\text{Current density}_{\text{ECSA}} = j \times C_s/C_{dl} \tag{4}$$

According to the surface concentration of active sites associated with the redox metal species and the linear relationship between the oxidation peak current and scan rate from the CV scans, turnover frequency (TOF) can be calculated using the following equation:

$$\mathrm{TOF} = \frac{\text{Number of total hydrogen turnovers per cm}^2}{\text{Number of active site per cm}^2} \quad (5)$$

The total number of hydrogen turnovers is calculated from the current density extracted from the LSV curve, as shown in the following formula:

$$n_{H2} = \left(|j|\frac{\text{mA}}{\text{cm}^2}\right)\left(\frac{1\text{C } s^{-1}}{1000\text{ mA}}\right)\left(\frac{1\text{ mol e}^-}{96485.3\text{ C}}\right)\left(\frac{1\text{ mol H}_2}{2\text{ mol e}^-}\right)\left(\frac{6.022\times10^{23}\text{ H}_2\text{ molecules}}{1\text{ mol H}_2}\right) = 3.12\times10^{15}\frac{\text{H}_2}{\text{cm}} \quad (6)$$

$$\frac{\text{mA}}{\text{cm}^2}$$

For simplicity, the total number of surface sites is recognized as the number of active sites. The volume of cell for Ni crystal structure is 43.46 Å^3. Therefore, the number of active sites per real surface area is calculated as follows:

$$n_{\text{active sites}} = \left(\frac{4\text{ atom/unit cell}}{43.46\text{ Å}^3\text{/unitcell}}\right)^{2/3} = 2.039\times10^{15}\text{ atoms per real cm}^2 \quad (7)$$

Finally, plots of current density for Ni can be converted into TOF plots according to:

$$TOF = \frac{(3.12 \times 10^{15} \frac{H_2/s}{cm^2}) per \frac{mA}{cm^2}) \times |j|}{(2.039 \times 10^{15} \text{ atoms per } cm^2) \times ECSA} \quad (8)$$

The accelerated degradation test (ADT) was conducted at a scan rate of 20 mV s^{-1} by performing cyclic voltammetry for 2000 continuous cycles for HER and OER, respectively. The long-term stability performance was measured using a simple chronopotentiometric measurement at a current density of 10 and 100 mA cm^{-2}, respectively. The amount of generated gases during bulk electrolysis was quantified by gas chromatography (GC, 8860 GC System, carrier gas: Ar; chromatographic column: 5 Å molecular sieve column; detector: TCD). Before each measurement, the electrolyte was bubbled with Ar for 30 min.

DFT calculations

The theoretical calculations were performed via density functional theory (DFT) by the Vienna Ab-initio Simulation Package (VASP). The Perdew-Burke-Ernzerhof (PBE) functional and the projector-augmented wave (PAW) were used for VASP.[7, 8] The convergence threshold for structural optimization was set as 10^{-5} eV in energy and -0.05 eV in force. Considering the planewave basis restriction, the cutoff energy was set as 450 eV. In this work, the Brillouin zone was sampled with the Monkhorst-Pack scheme. Monkhorst-Pack k-point setups were 3 × 3 × 3 and 3 × 3 × 1 for bulk and slab geometry optimization, respectively.

The hydrogen adsorption Gibbs free energy ΔG_H can be achieved as follows:

$$\Delta G_H = \Delta E_H + \Delta E_{zpe} - T\Delta S_H \quad (9)$$

Where ΔG_{H*} represents the adsorption energy of H. ΔE_{zpe} and $T\Delta S_H$ represent the difference of the zero-point energy and entropy between the hydrogen adsorbed state and the gas phase H_2. Moreover, the overall contribution can be rewritten as:[3]

$$\Delta G_H = \Delta E_H + 0.24 = E_{(surf+H)} - E_{(surf)} - 1/2E_{(H2)} + 0.24 \quad (10)$$

The OER performance of the catalysts was determined by the relative energy of the intermediates OH, O, OOH and O_2 in alkaline environments:[9]

$$* + H_2O \rightarrow *OH + (H^+ + e^-) \quad (11)$$

$$*OH \rightarrow *O + (H^+ + e^-) \quad (12)$$

$$*O + H_2O \rightarrow *OOH + (H^+ + e^-) \quad (13)$$

$$*OOH \rightarrow O_2 + (H+ + e^-) \quad (14)$$

where * represents adsorption sites. The relative energy of each step is obtained by

$$\text{Relative energy} = \Delta E_H + \Delta ZPE - T\Delta S \quad (15)$$

where ΔE_H is the calculated total energy difference, ΔZPE and $T\Delta S$ is zero-point energy correction and entropy difference, respectively.

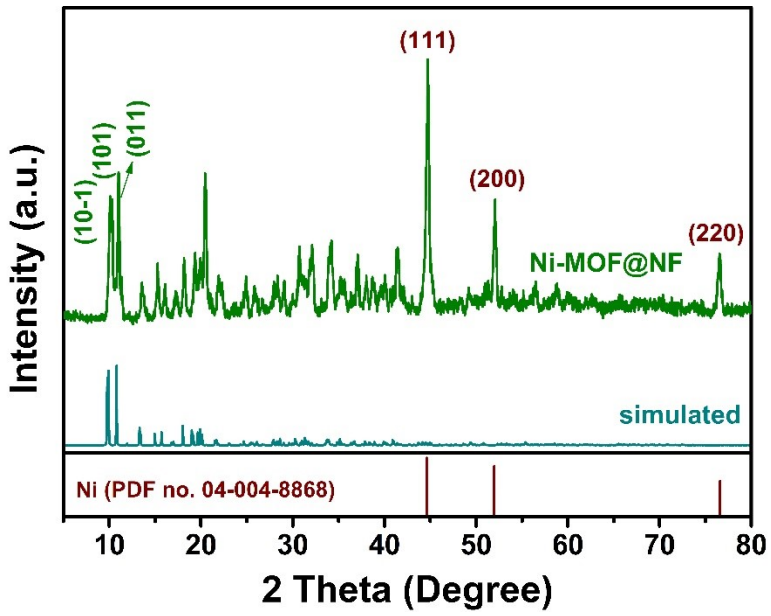

Fig. S1 The XRD patterns of as-prepared Ni-MOF@NF precursor.

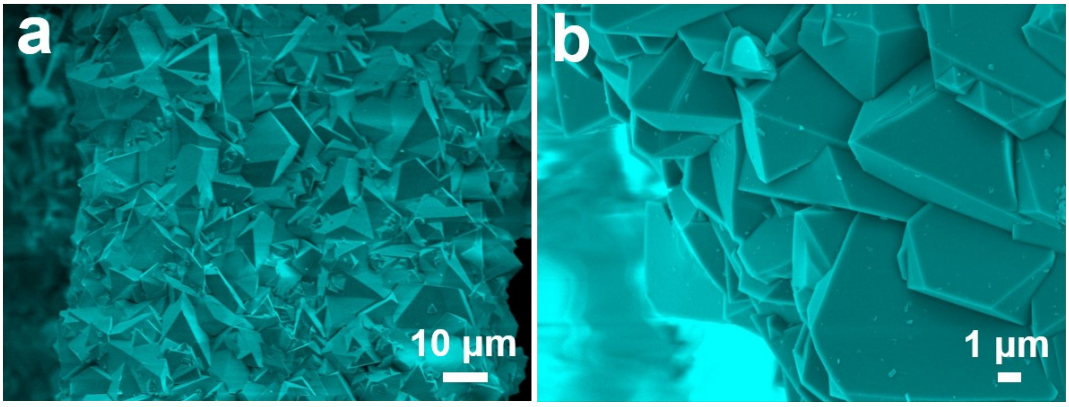

Fig. S2 The SEM images of Ni-MOF@NF precursor.

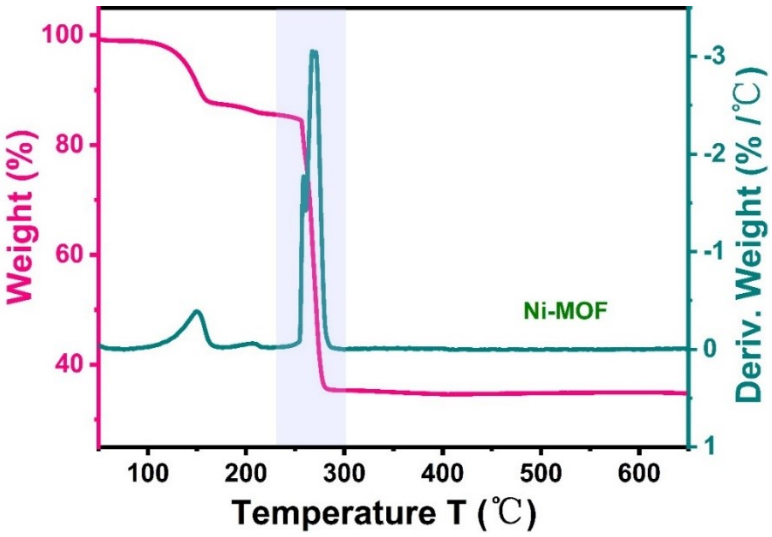

Fig. S3 The TGA curves of Ni-MOF@NF precursor.

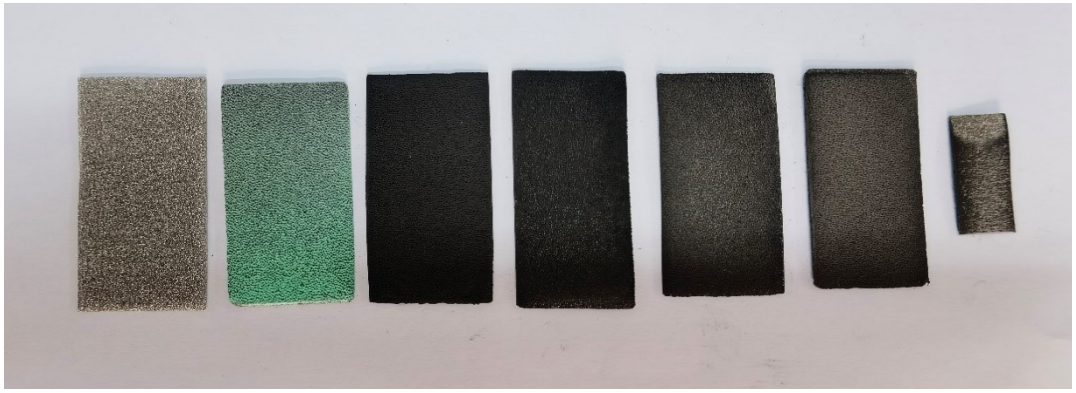

Fig. S4 The digital photos of the samples at different preparation stages. From left to right is bare NF, Ni-MOF@NF precursor, Ni-250-2@NF, Ni-250-12@NF, Ni-400@NF, Ni-550@NF and p-Ni@NF, respectively.

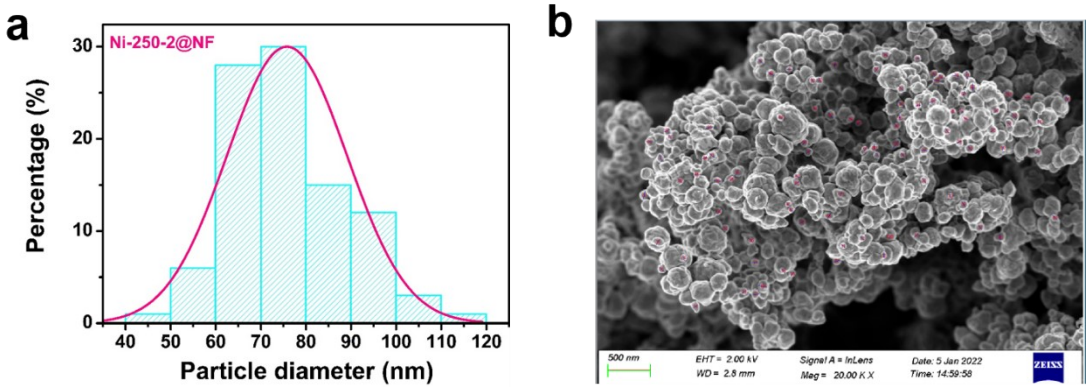

Fig. S5 (a) The particle dimensions distribution histogram. (b) SEM image for particle diameter statistics of Ni-250-2@NF.

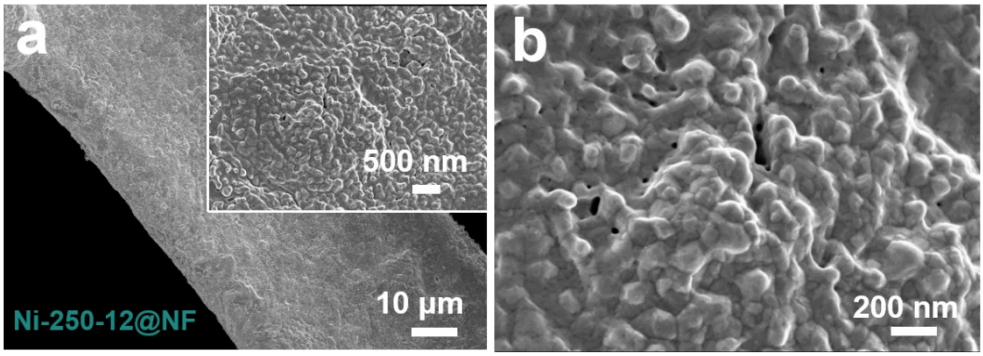

Fig. S6 (a) Low- and (b) high-magnification SEM images of Ni-250-12@NF. Inset is the enlarged view.

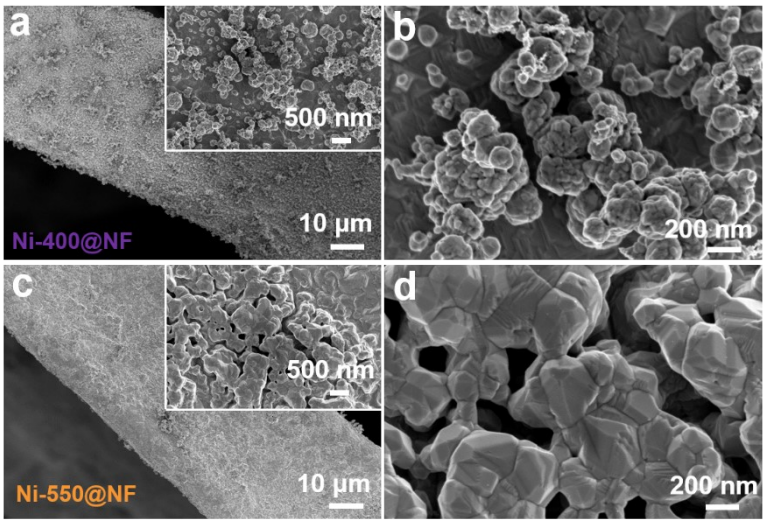

Fig. S7 SEM images of the calcinated products at different temperatures. (a, b) Ni-400@NF. (c, d) Ni-550@NF.

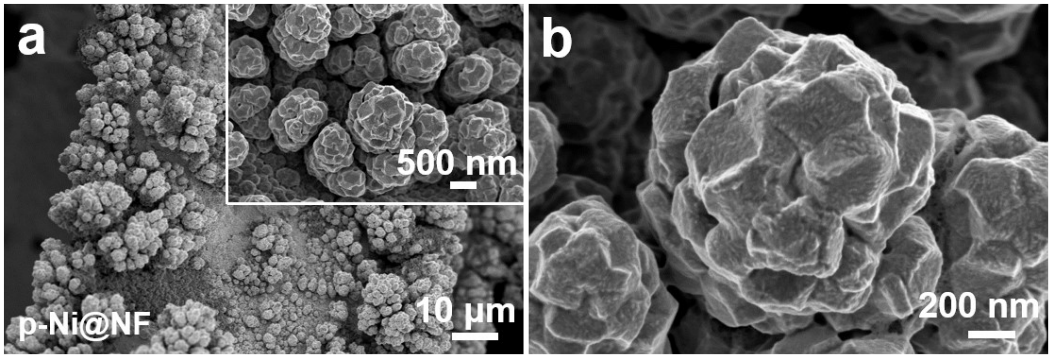

Fig. S8 (a) Low- and (b) high-magnification SEM images of p-Ni@NF sample. Inset is the enlarged view.

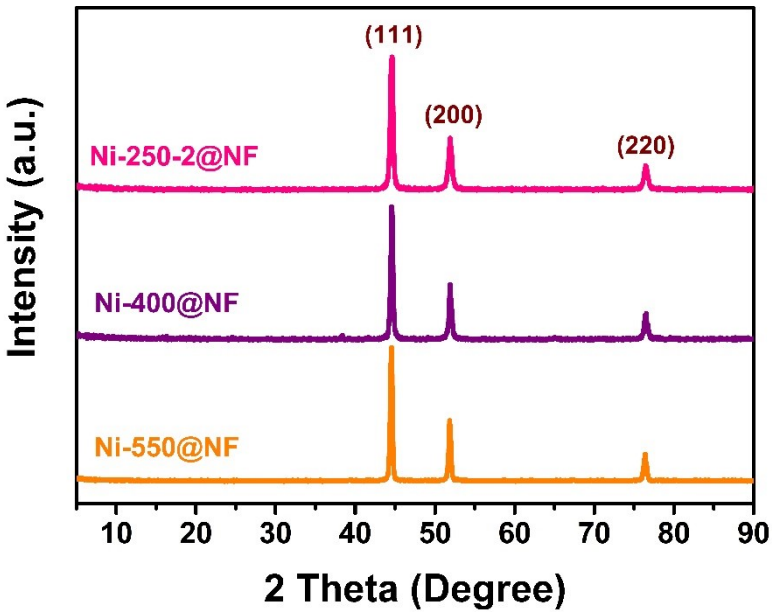

Fig. S9 The XRD patterns of as-prepared Ni-250-2@NF, Ni-400@NF and Ni-550@NF.

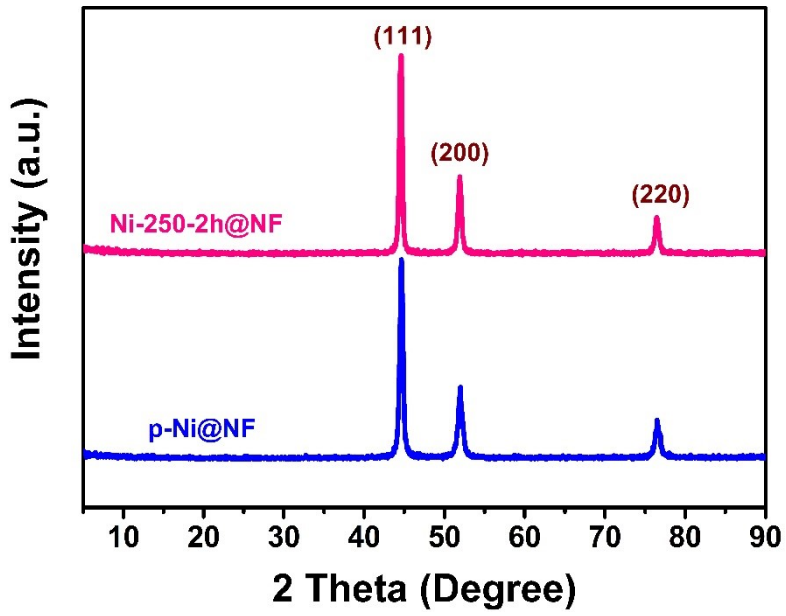

Fig. S10 The XRD patterns of as-prepared Ni-250-2@NF and p-Ni@NF.

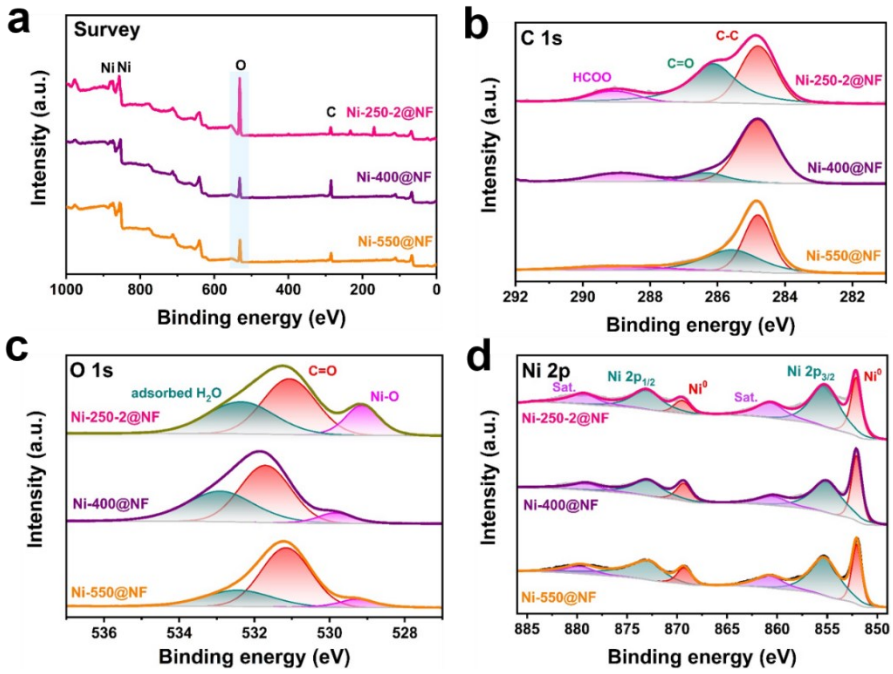

Fig. S11 The XPS spectra of the Ni-250-2@NF, Ni-400@NF and Ni-550@NF.

(a) Survey. (b) C 1s. (c) O 1s. (d) Ni 2p.

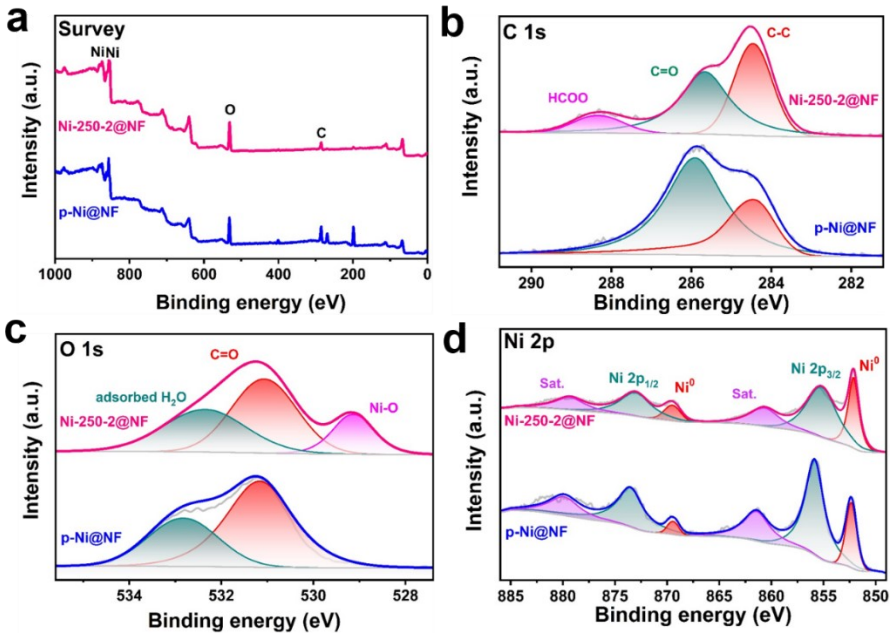

Fig. S12 The XPS spectra of the Ni-250-2@NF and p-Ni@NF.

(a) Survey. (b) C 1s. (c) O 1s. (d) Ni 2p.

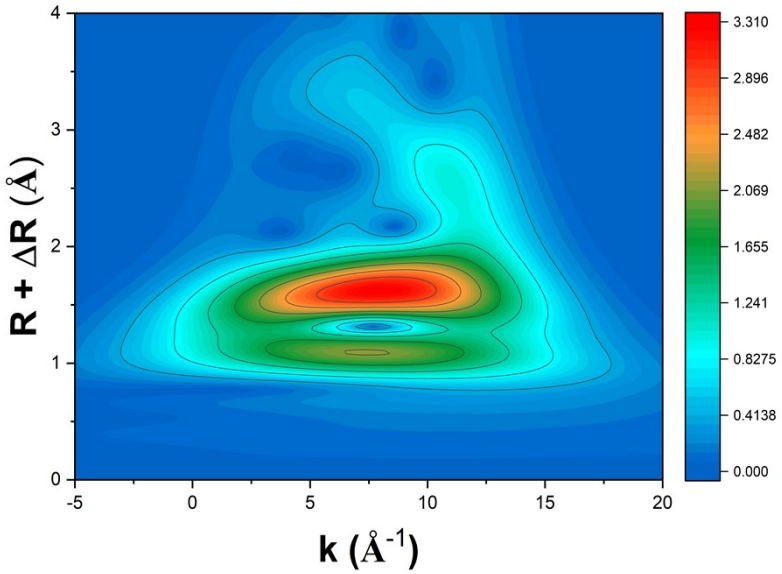

Fig. S13 WT contour plots of Ni K-edge at R space of Ni-MOF@NF precursor.

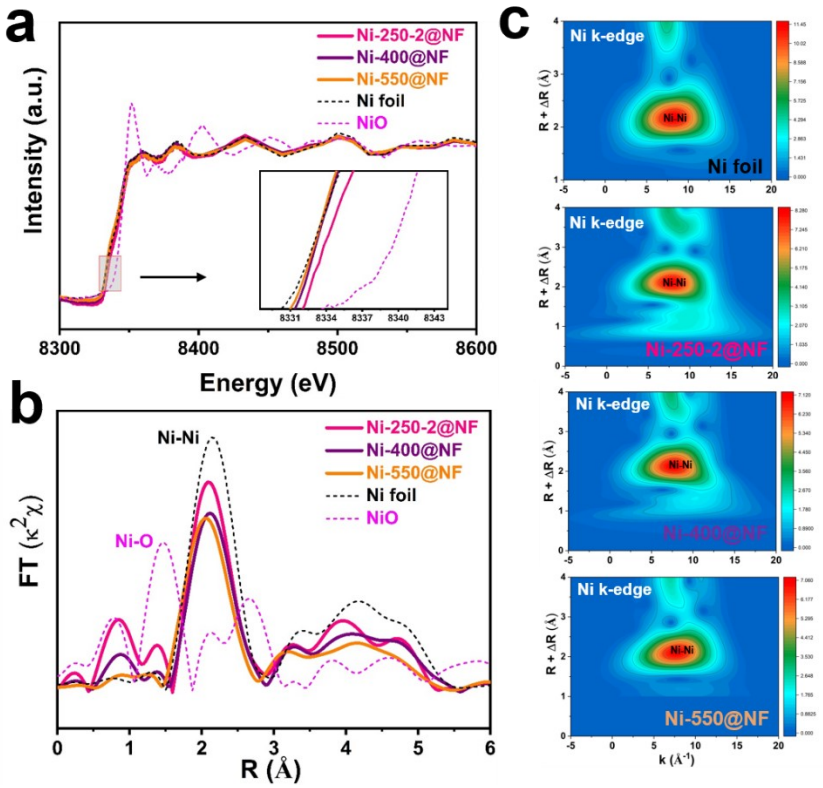

Fig. S14 (a) The normalized Ni K-edge XANES spectra. (b) FT-EXAFS spectra of Ni-250-2@NF, Ni-400@NF, Ni-550@NF, Ni foil and NiO. (c) WT contour plots of Ni K-edge at R space of Ni-250-2@NF, Ni-400@NF, Ni-550@NF and Ni foil.

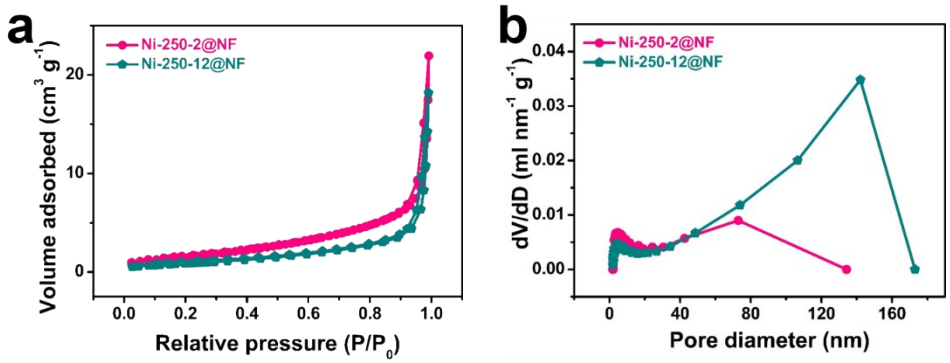

Fig. S15 (a) N_2 adsorption-desorption isotherms. (b) Pore-size distribution of Ni-250-2@NF and Ni-250-12@NF.

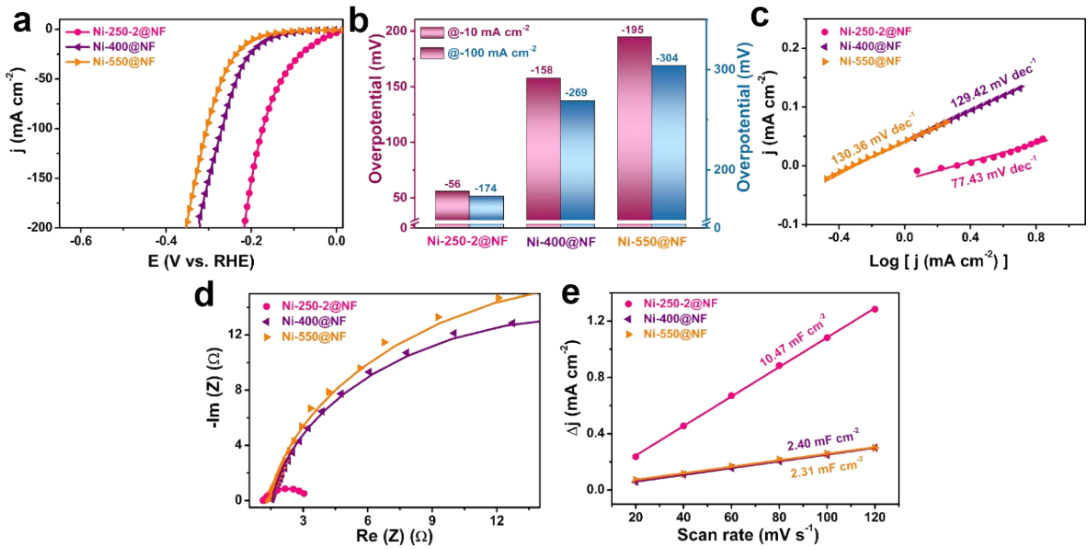

Fig. S16 (a) HER polarization curves. (b) Bar graph of the overpotentials (η) at 10 mA cm^{-2} and 100 mA cm^{-2}, respectively. (c) Tafel plots. (d) Nyquist plots. (e) The capacitive currents in the middle of the potential window as a function of scan rate for Ni-250-2@NF, Ni-400@NF and Ni-550@NF.

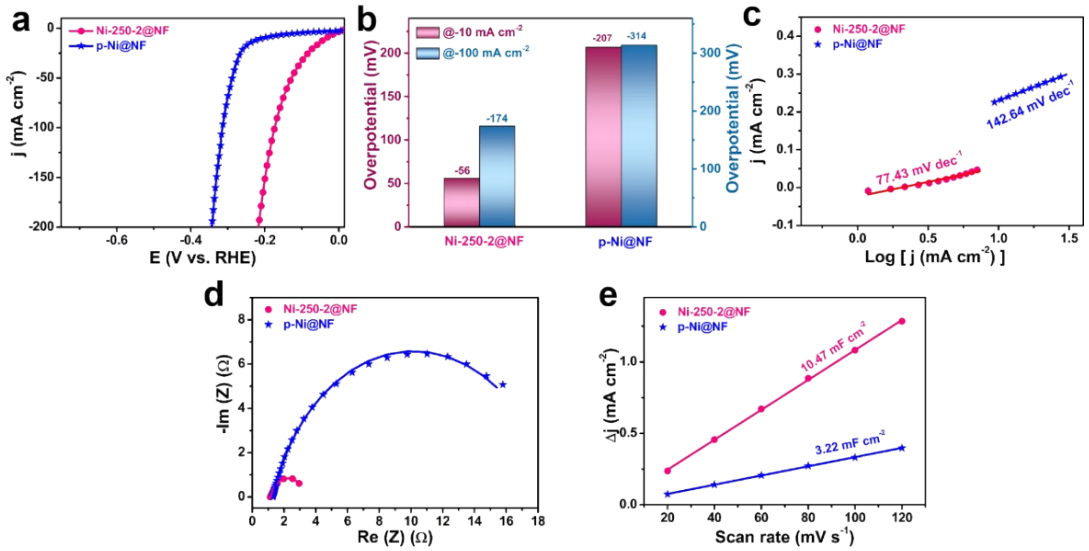

Fig. S17 (a) HER polarization curves. (b) Bar graph of the overpotentials (η) at 10 mA cm^{-2} and 100 mA cm^{-2}, respectively. (c) Tafel plots. (d) Nyquist plots. (e) The capacitive currents in the middle of the potential window as a function of scan rate for Ni-250-2@NF and p-Ni@NF.

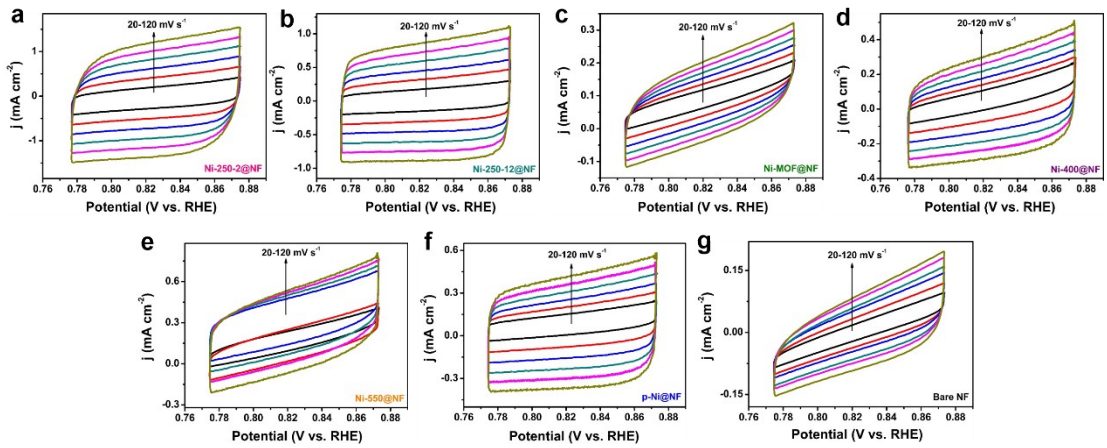

Fig. S18 CV curves showing the capacitive behaviors of electrochemical double layer of (a) Ni-250-2@NF, (b) Ni-250-12@NF, (c) Ni-MOF@NF, (d) Ni-400@NF, (e) Ni-550@NF, (f) p-Ni@NF and (g) bare NF.

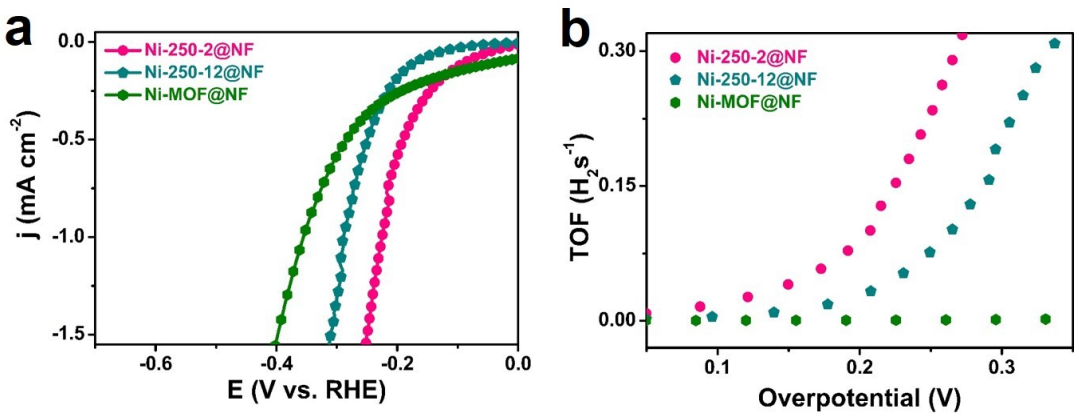

Fig. S19 (a) ECSA-normalized LSV curves and (b) plot of TOF as a function of overpotential for Ni-250-2@NF, Ni-250-12@NF and Ni-MOF@NF toward the HER.

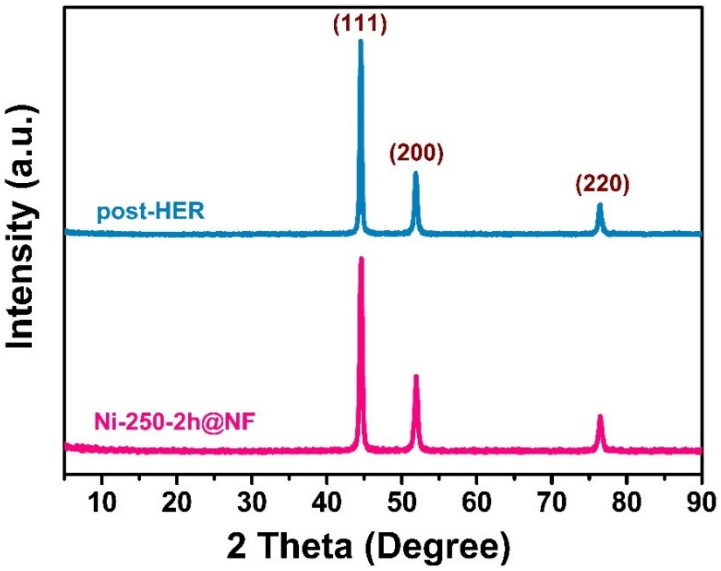

Fig. S20 XRD patterns of the Ni-250-2@NF after long-term HER process in alkaline electrolyte.

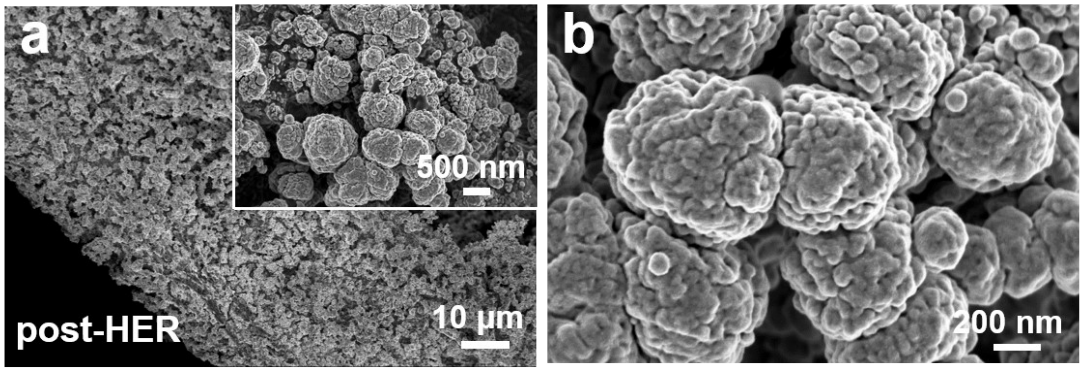

Fig. S21 SEM images of the Ni-250-2@NF after long-term HER process in alkaline electrolyte.

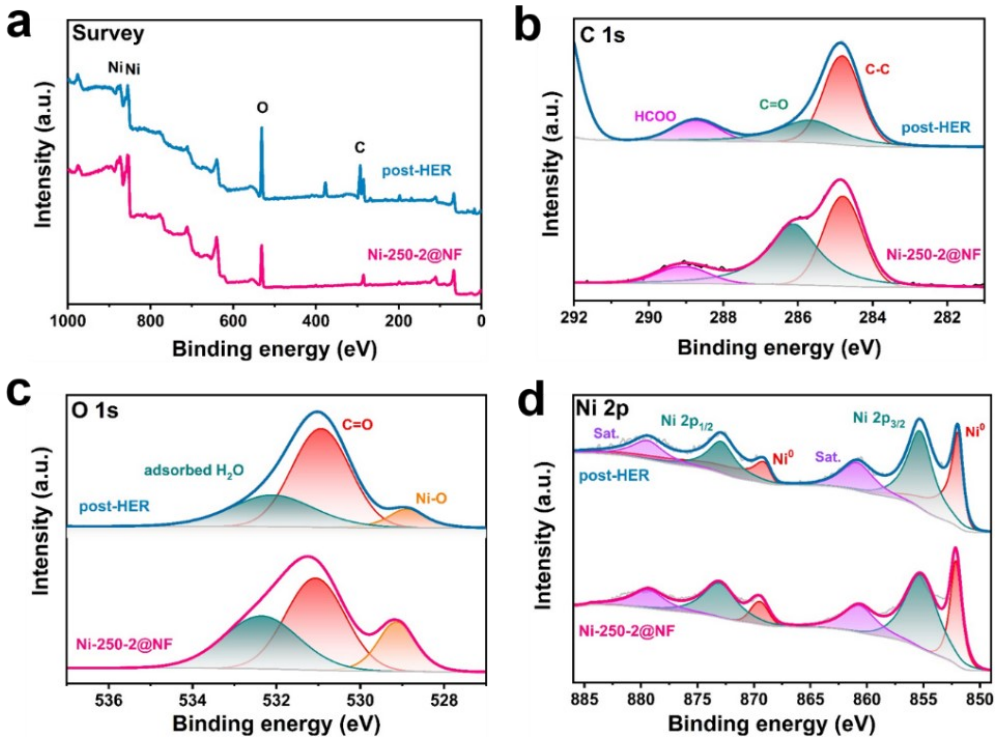

Fig. S22 XPS spectra of the Ni-250-2@NF before and after HER process (post-HER) in alkaline electrolyte. (a) Survey. (b) C 1s. (c) O 1s. (d) Ni 2p.

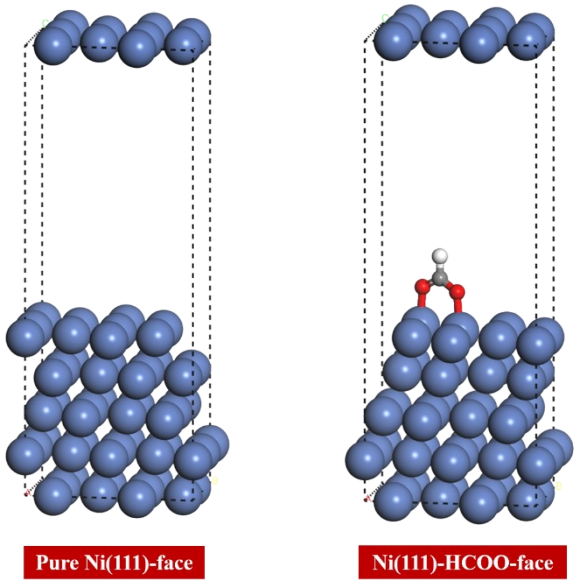

Fig. S23 The models of the Pure Ni(111)-face and Ni(111)-HCOO-face. The bluish grey, red, grey and light grey represents the Ni atom, O atom, C atom and H atom, respectively.

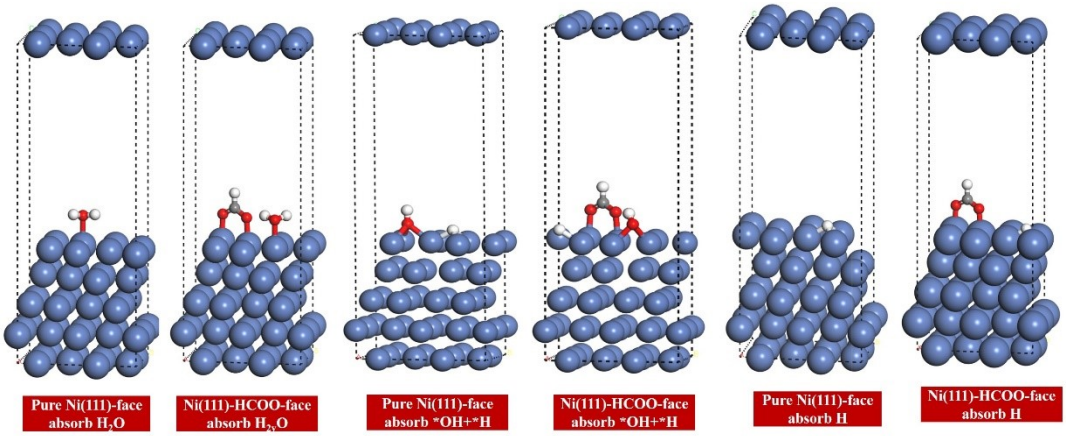

Fig. S24 The models of *H_2O, *OH+*H and *H atoms on the Pure Ni(111)-face and Ni(111)-HCOO-face, respectively.

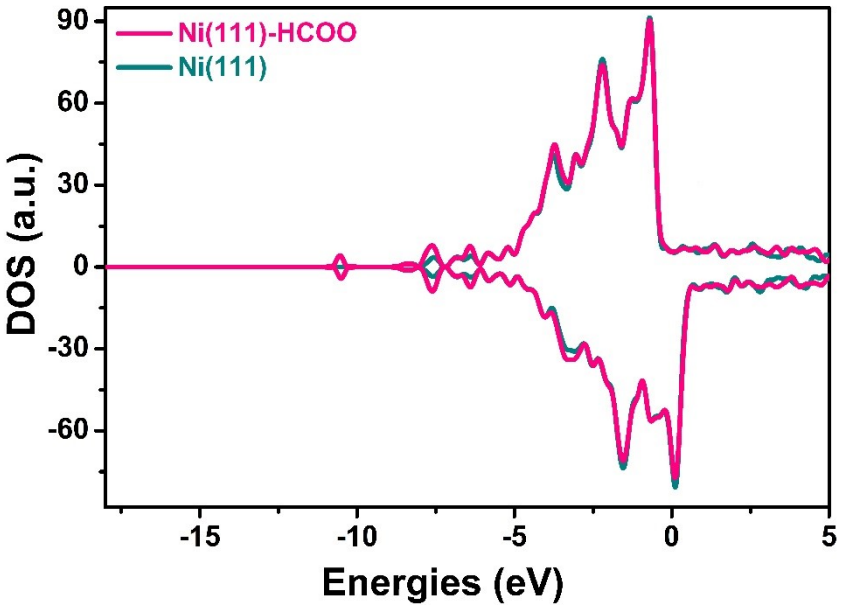

Fig. S25 Total density of states (DOS) of Ni(111) and Ni(111)-HCOO.

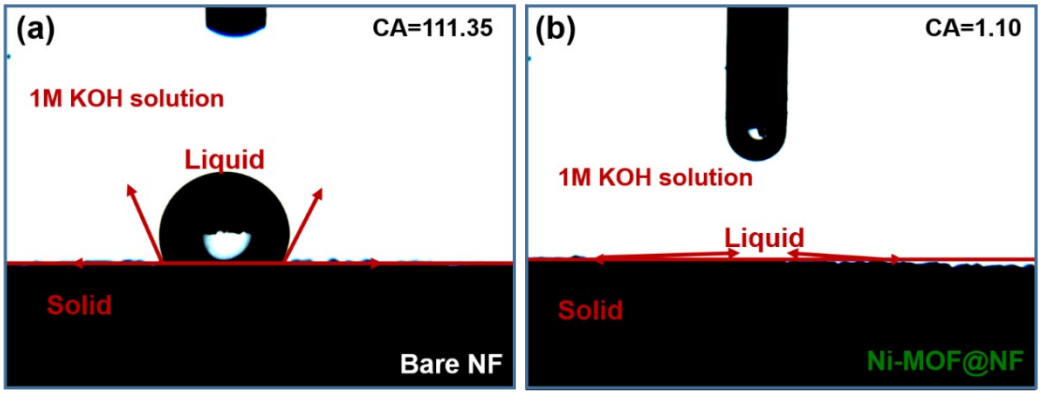

Fig. S26 Contact angles of (a) Bare NF and (b) Ni-MOF@NF.

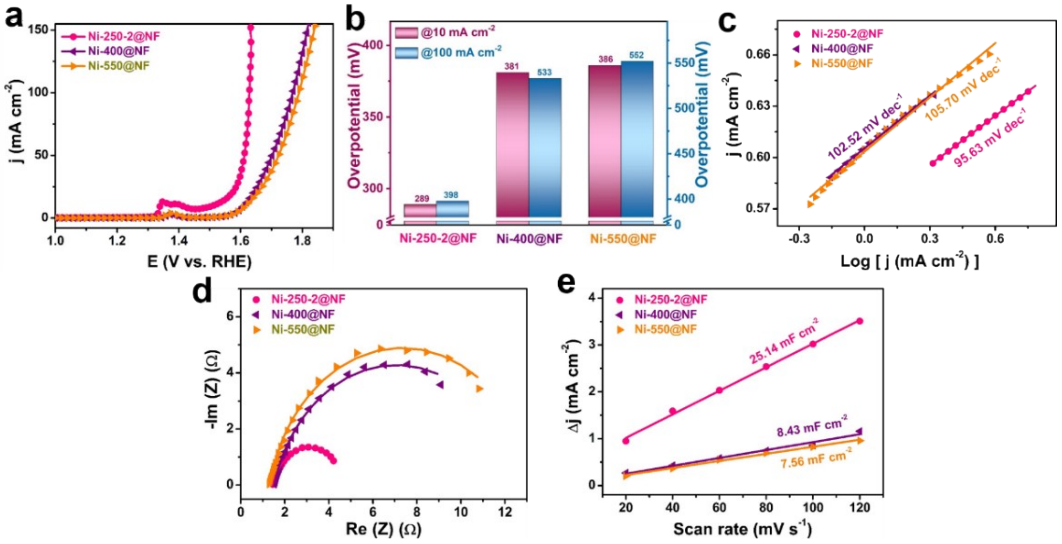

Fig. S27 (a) OER polarization curves. (b) Bar graph of the overpotentials (η) at 10 mA cm^{-2} and 100 mA cm^{-2}, respectively. (c) Tafel plots. (d) Nyquist plots. (e) The capacitive currents in the middle of the potential window as a function of scan rate for Ni-250-2@NF, Ni-400@NF and Ni-550@NF.

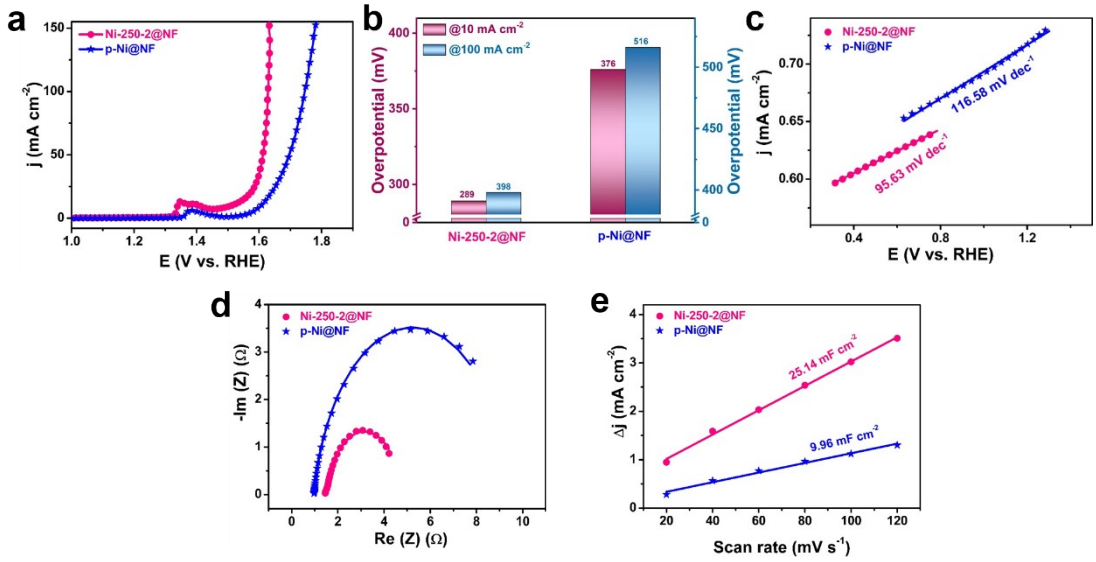

Fig. S28 (a) OER polarization curves. (b) Bar graph of the overpotentials (η) at 10 mA cm^{-2} and 100 mA cm^{-2}, respectively. (c) Tafel plots. (d) Nyquist plots. (e) The capacitive currents in the middle of the potential window as a function of scan rate for Ni-250-2@NF and p-Ni@NF.

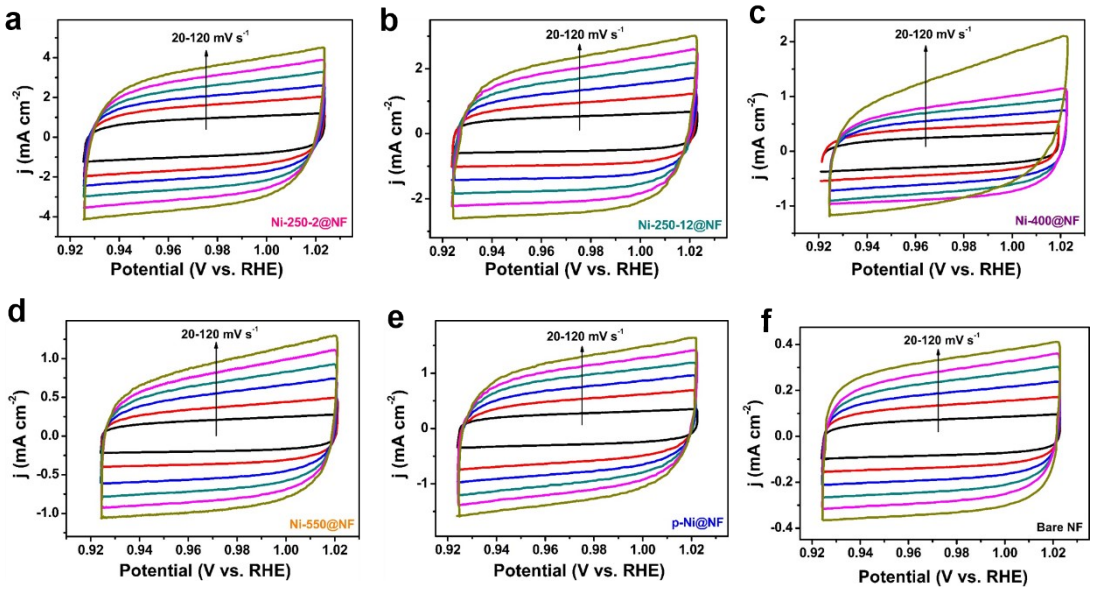

Fig. S29 CV curves showing the capacitive behaviors of electrochemical double layer of (a) Ni-250-2@NF, (b) Ni-250-12@NF, (c) Ni-400@NF, (d) Ni-550@NF, (e) p-Ni@NF and (f) bare NF.

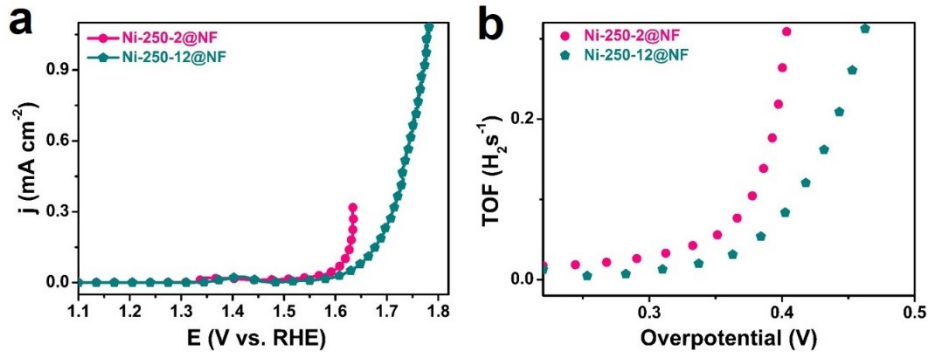

Fig. S30 (a) ECSA-normalized LSV curves and (b) plot of TOF as a function of overpotential for Ni-250-2@NF and Ni-250-12@NF toward the OER.

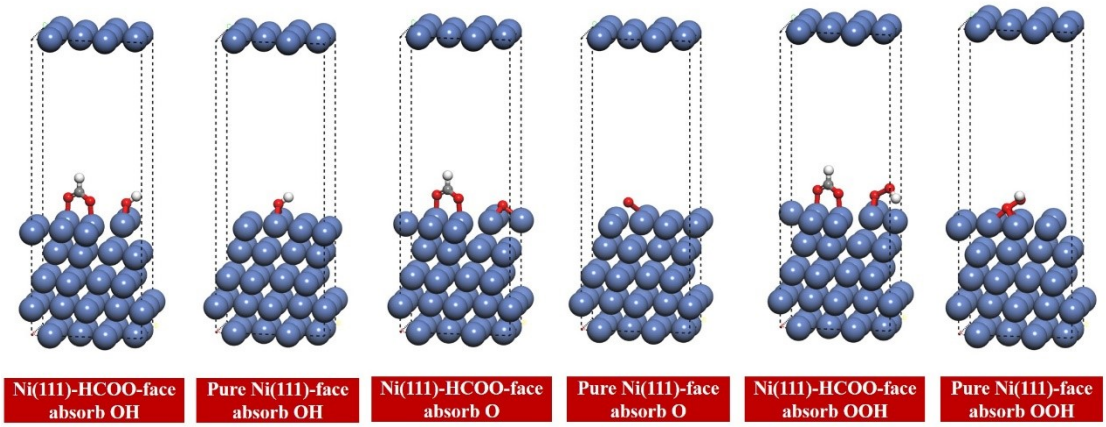

Fig. S31 The models of *OH, *O and *OOH atoms on the Ni(111)-HCOO-face and Pure Ni(111)-face, respectively.

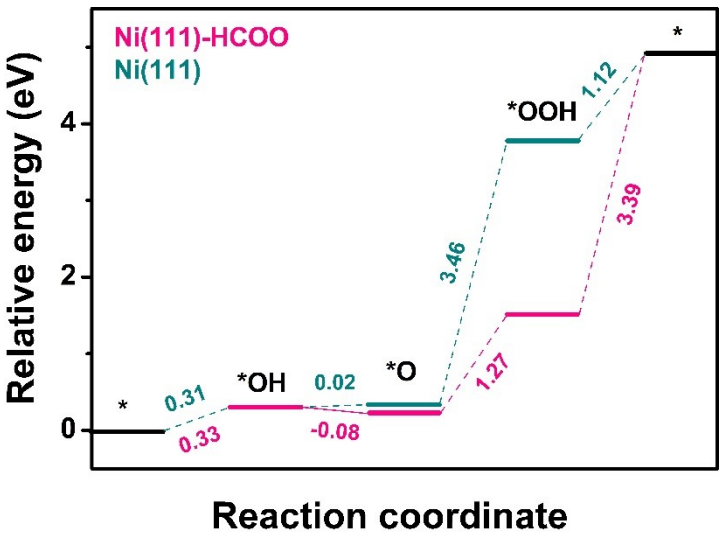

Fig. S32 Energy profiles of the four-electron OER mechanism and corresponding side-view intermediate structures on the Ni(111) and Ni(111)-HCOO.

To further investigate and understand the OER mechanism, the adsorption Gibbs free energy (ΔG) on the Ni(111) and Ni(111)-HCOO are investigated by DFT calculations (Fig. S32), which includes the absorption energies of intermediates *OH, *O and *OOH intermediate. The optimized structures with adsorbed intermediates for OER are illustrated in Fig. S31. As for OER process, the largest ΔG is related to the rate-determining step (RDS). For the (111) plane of Ni (Ni(111)), the RDS Gibbs free energy is the intermediate reaction from O* to OOH*, and the corresponding energy barrier is reduced 3.46 eV (ΔGOOH*). However, the OER process for Ni(111)-HCOO displayed the last oxidation step (OOH*→ O_2) becomes the RDS, and the RDS Gibbs free energy of Ni(111)-HCOO is 3.39 eV (ΔG_{O2}) to achieve the water oxidation. This means that the existence of HCOO (Ni(111)-HCOO) can optimize and reduced the RDS towards OER.

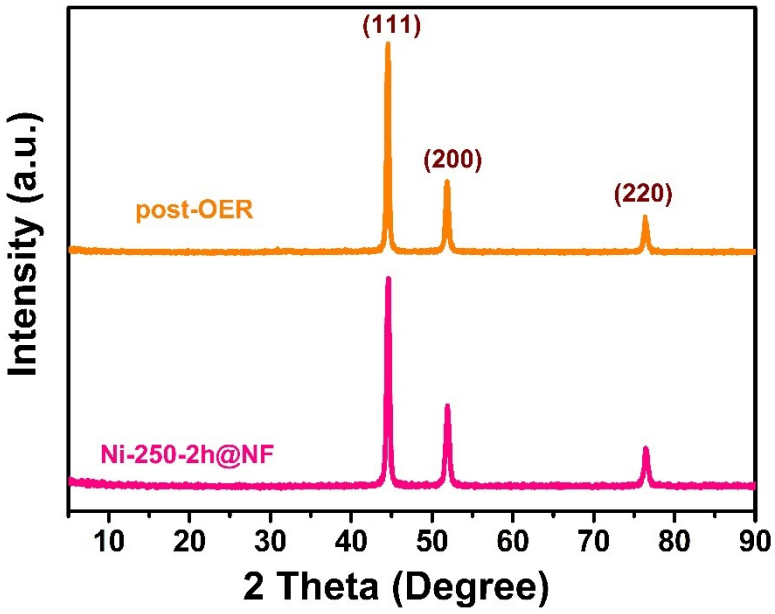

Fig. S33 XRD patterns of the Ni-250-2@NF after long-term OER process in alkaline electrolyte.

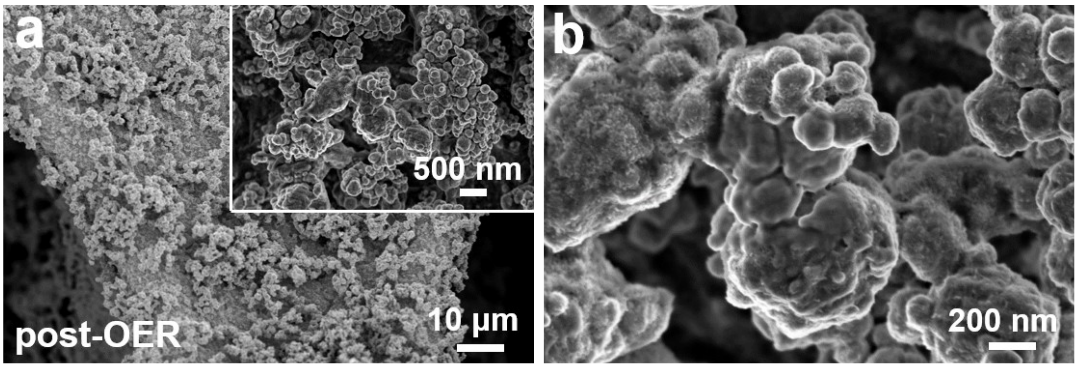

Fig. S34 SEM images of the Ni-250-2@NF after long-term OER process in alkaline electrolyte.

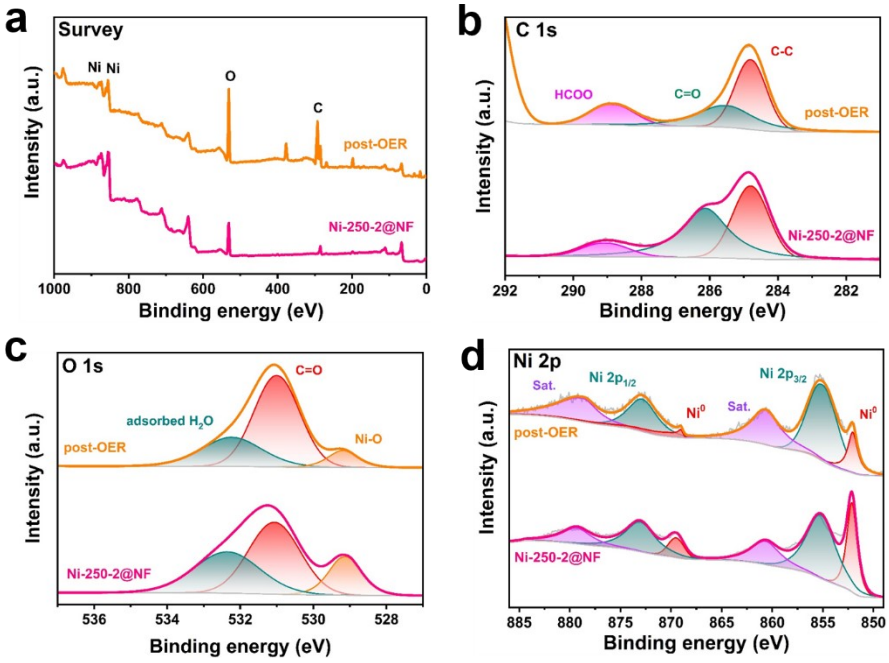

Fig. S35 XPS spectra of the Ni-250-2@NF before and after OER reaction (post-OER) in alkaline electrolyte. (a) Survey. (b) C 1s. (c) O 1s. (d) Ni 2p.

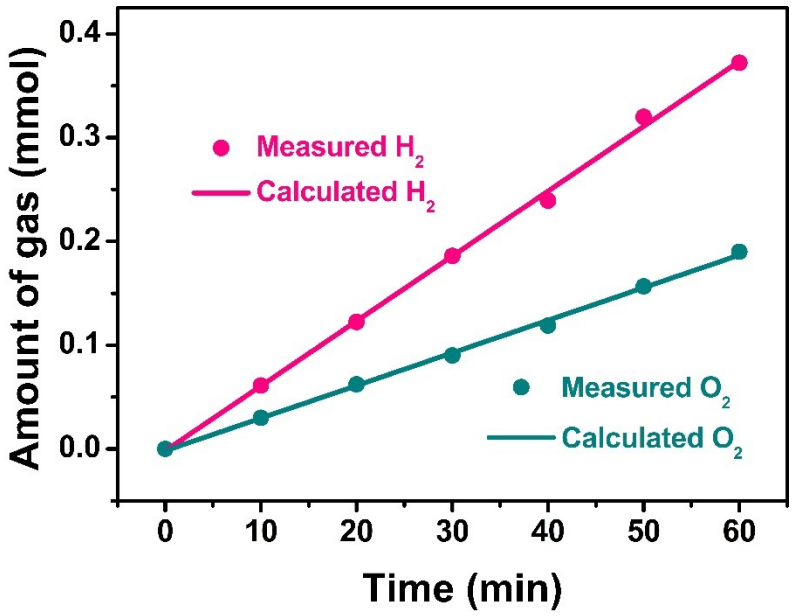

Fig. S36 The amount of H_2 and O_2 gas theoretically calculated and experimentally measured versus time at the current density of 10 mA cm^{-2} for Ni-250-2@NF.

Table S1. Quantitative analysis of Ni-MOF@NF precursor, Ni-250-2@NF and Ni-250-12@NF from XPS measurements.

	Ni-MOF@NF precursor	**Ni-250-2@NF**	**Ni-250-12@NF**
C 1s (CPS.eV)	88006.97	21767.54	26483.62
HCOO (CPS.eV)	49461.71 (56%)	2635.51 (12%)	539.41 (2%)
O 1s (CPS.eV)	279059.46	100469.58	155906.9
Ni-O (CPS.eV)	-	16899.05 (16%)	3612.72 (2%)

Table S2. Comparison of electrocatalytic HER performance for Ni-250-2@NF with other recently reported catalysts in alkaline electrolyte.

Catalyst	Electrolyte	η_{10} (mV)	η_{100} (mV)	Tafel slope (mV dec-1)	Reference
Ni-250-2@NF	1.0 M KOH	56	174	77.43	This work
NiS/G-3	1.0 M KOH	70	-	50.1	10
NiFe-MS/MOF@NF	1.0 M KOH	90	-	82	11
N-doped Ni_5P_4	1.0 M KOH	96	-	62.2	12
NiS_2/MoS_2	1.0 M KOH	102	-	67	13
N-$NiMoO_4/NiS_2$	1.0 M KOH	99	-	74.2	14
Ni_3S_2	1.0 M KOH	50	-	67	15
NiO_x-Cat/FTO	0.5 M KOH	350	-	89	16
$NiCo_2Se_4/NiCoS_4$	1.0 M KOH	180	-	107.4	17
Ni_3S_2-MoS_2 NWAs/NF	1.0 M KOH	99	260	65	18
Ni-Mo-N	1.0 M KOH	55	125	61.4	19
Ni-Sv-MoS_2	1.0 M KOH	101	-	66	20
Ni–Co–P HNBs	1.0 M KOH	107	-	46	21
Co/CoN/Co_2P-NPC	1.0 M KOH	99	-	51	22
CoP@FeCoP/NC YSMPs	1.0 M KOH	141	-	56.34	23

Table S3. EIS parameters (R_s and R_{ct}) of catalysts for the HER at controlled-potential of -0.126 V vs. RHE.

catalysts	R_s (Ω)	R_{ct} (Ω)
Ni-250-2@NF	1.169	2.19
Ni-250-12@NF	1.454	3.08
Ni-400@NF	1.558	30.13
Ni-550@NF	1.407	36.96
p-Ni@NF	1.298	34.60
Ni-MOF@NF	2.374	60.80
Pt/C/NF	1.068	1.36
NF	1.712	34.60

Table S4. Comparison of double layer capacitance (C_{dl}) and electrochemical active surface area (ECSA) of as-synthesized samples for HER.

Catalysts	C_{dl} (mF cm^{-2})	ECSA (cm^2)
Ni-250-2@NF	10.47	261.75
Ni-250-12@NF	7.13	178.25
Ni-400@NF	2.40	60.00
Ni-550@NF	2.31	57.75
p-Ni@NF	3.22	80.50
Ni-MOF@NF	0.95	23.75
NF	0.69	17.25

Table S5. Comparison of electrocatalytic OER performance for Ni-250-2@NF with other recently reported catalysts in alkaline electrolyte.

Catalyst	Electrolyte	η_{10} (mV)	Tafel slope (mV dec^{-1})	Reference
Ni-250-2@NF	1.0 M KOH	289	95.63	This work
Fe/Fe_3C-MC	1.0 M KOH	320	51	24
Ni_3C/NC	1.0 M KOH	309	72	25
Fe-Ni_3C-2%	1.0 M KOH	292	41.3	26
NiS/G-3 2D	1.0 M KOH	300	55.8	10
Fe-Co_3O_4 HHNPs	1.0 M KOH	262	43	27
Ni_3S_2	1.0 M KOH	295	52	15
NiO	1.0 M KOH	310	54	28
NiO_xSC/FTO	0.5 M KOH	300	89	16
$NiCo_{16-x}P_6$	1.0 M KOH	290	66	29
Ni-Co-P HNBs	1.0 M KOH	270	76	21
$Co/CoN/Co_2P$-NPC	1.0 M KOH	272	62	22
CoP@FeCoP/NC YSMPs	1.0 M KOH	238	47.89	23

Table S6. EIS parameters (R_s and R_{ct}) of catalysts for the OER at controlled-potential of 1.604 V vs. RHE.

Catalysts	R_s (Ω)	R_{ct} (Ω)
Ni-250-2@NF	1.477	3.34
Ni-250-12@NF	1.479	5.77
Ni-400@NF	1.528	11.07
Ni-550@NF	1.318	12.02
p-Ni@NF	1.298	8.54
RuO_2/NF	1.218	2.64
NF	1.498	43.25

Table S7. Comparison of double layer capacitance (C_{dl}) and electrochemical active surface area (ECSA) of as-synthesized samples for OER.

Catalysts	C_{dl} (mF cm^{-2})	ECSA (cm^2)
Ni-250-2@NF	25.14	628.50
Ni-250-12@NF	18.45	461.25
Ni-400@NF	8.43	210.75
Ni-550@NF	7.56	189.00
p-Ni@NF	9.96	249.00
NF	2.55	63.75

References

1 S. Wang, Q. Guo, S. Liang, P. Li, X. Li and J. Luo, *Chem. Eng. Technol*., 2018, **41**, 353-366.

2 Z.H. Wan, Z.Z. Ma, H.F. Yuan, K. Liu and X.G. Wang, *ACS Appl. Energy Mater*., 2022, **5**, 4603-4612.

3 H. Yuan, S. Zheng, S. Sang, J. Yang, J. Sun, Z. Ma and X. Wang, *Int. J. Hydrog. Energy*, 2022, **47**, 11827-11840.

4 S.M. Wang, Y. Zhang, X.Y. Deng, Z.Z.Ma, H.F. Yuan, J.P. Li and X.G. Wang, Int. J. Hydrog. Energy, 2022, **47**, 40932-40942.

5. L. Yan, H.Y. Wanga, J.L. Shen, J.Q. Ning, Y.J. Zhong and Y. Hu, Chem. Eng. J., 2021, **403**, 126385.

6. Y.H. Song, M.X. Song, P.Z. Liu, W.W. Liu, L.J. Yuan, X.D. Hao, L.Y. Pei, B.S. Xu, J.J. Guo and Z.Q. Sun, J. Mater. Chem. A, 2021, **9**, 14372.

7 L.W. Jiang, Y. Huang, Y. Zou, C. Meng, Y. Xiao, H. Liu and J.J. Wang, *Adv. Energy Mater*., 2022, **12**, 2202351.

8 Z.X. Wu, Y. Zhao, H.B. Wu, Y.X. Gao, Z. Chen, W. Jin, J.S. Wang, T.Y. Ma and L. Wang, *Adv. Funct. Mater*., 2021, **31**, 2010437.

9. H.H. Zhang, Y.Y. Liu, T. Chen, J.T. Zhang, J. Zhang and X. W. (David) Lou, Adv. Mater. 2019, 31, 1904548.

10 D. Zhang, H. Mou, F. Lu, C. Song and D. Wang, *Appl. Catal. B*, 2019, **254**, 471-478.

11 M. Zhao, W. Li, J. Li, W. Hu and C.M. Li, *Adv. Sci.*, 2020, **7**, 2001965.

12 G.Y. Zhou, Y.R. Ma, X.M. Wu, Y.Z. Lin, H. Pang, M.Y. Zhang, L. Xu, Z.Q. Tian and Y.W. Tang, *Chem.Eng. J*., 2020, **402**, 126302.

13 J. Wang, Z. Liu, C. Zhan, K. Zhang, X. Lai, J. Tu and Y. Cao, *J. Mater. Sci. Technol*., 2020, **39**, 155-160.

14 L. An, J.R. Feng, Y. Zhang, R. Wang, H.W. Liu, G.C. Wang, F.Y. Cheng and P.X. Xi, *Adv. Funct. Mater*., 2019, **29**, 1805298.

15 X. Zheng, X. Han, Y. Zhang, J. Wang, C. Zhong, Y. Deng and W. Hu, *Nanoscale*,

2019, **11**, 5646-5654.

16 N.U. Babar and K.S. Joya, *ACS Omega*., 2020, **5**, 10641-10650.

17 K.K. Wang, Z.S. Lin, Y. Tang, Z.H. Tang, C.L. Tao, D.D. Qin and Y. Tian, *Electrochim. Acta*, 2021, **368**, 137584.

18 S.Z. Xundi Gu, Xiaobo Huang, Hefeng Yuan, Jinping Li, Manab Kundu and Xiaoguang Wang, *ChemComm.* 2020, **56**, 2471-2474

19 Z.N. Wang, J. Lu, S. Ji, H. Wang, X.Y. Wang, B.G. Pollet and R.F. Wang, J. Alloys Compd., 2021, **867**, 158983.

20 Y. Ma, D. Leng, X. Zhang, J. Fu, C. Pi, Y. Zheng, B. Gao, X. Li, N. Li, P.K. Chu, Y. Luo and K. Huo, *Small*, 2022, **18**, 2203173.

21 E.L. Hu, Y.F. Feng, J.W. Nai, D. Zhao, Y. Hu and X. W. (David) Lou, Energy Environ. Sci., 2018, **11**, 872.

22 L. Hu, Y.W. Hu, R. Liu, Y.C. Mao, M.-S. (J.T.) Balogun and Y.X. Tong, Int. J. Hydrog. Energy, 2019, **44**, 11402-11410.

23 J.H. Shi, F. Qiu, W.B. Yuan, M.M. Guo and Z.H. Lu, Chem. Eng. J., 2021, **403**, 126312.

24 X. Liang, J. Xiao, W. Weng and W. Xiao, *Angew. Chem. Int. Ed. Engl*., 2020, ***60***, 2120-2124.

25 J. Hao, G.F. Zhang, Y.T. Zheng, W.H. Luo, C. Jin, R. Wang, Z. Wang and W.J. Zheng, *Electrochim. Acta*, 2019, **320**, 134631.

26 H. Fan, H. Yu, Y. Zhang, Y. Zheng, Y. Luo, Z. Dai, B. Li, Y. Zong and Q. Yan, Angew. Chem. Int. Ed. Engl., 2017, **56**, 12566-12570.

27 S.L. Zhang, B.Y. Guan, X.F. Lu, S. Xi, Y. Du and X.W.D. Lou, *Adv. Mater.*, 2020, **32**, 2002235.

28 P.T. Babar, A.C. Lokhande, M.G. Gang, B.S. Pawar, S.M. Pawar and J.H. Kim, *J. Ind. Eng. Chem*., 2018, **60**, 493-497.

29 Y. Zhao, J. Zhang, Y. Xie, B. Sun, J. Jiang, W.J. Jiang, S. Xi, H.Y. Yang, K. Yan, S. Wang, X. Guo, P. Li, Z. Han, X. Lu, H. Liu and G. Wang, *Nano Lett.*, 2021, **21**, 823-832.